

Article

The Relationship between Granitic Magma and Mineralization in the Darongxi Skarn W Deposit, Xiangzhong District, South China: Constrained by Zircon and Apatite

Lei Cai ¹, Wei Li ^{2,*}, Guiqing Xie ¹ and Fangyuan Yin ¹

¹ Institute of Earth Sciences, China University of Geosciences, Beijing 100083, China; cl1344607955@163.com (L.C.); xieguiqing@cugb.edu.cn (G.X.)

² MNR Key Laboratory for Exploration Theory and Technology of Critical Mineral Resources, China University of Geosciences, Beijing 100083, China

* Correspondence: liwei2012cugb@163.com

Abstract: The Xiangho Zng district is the largest low-temperature W-Au-Sb metallogenic area in the world. The Darongxi skarn W deposit in the north of the Xiangzhong district is closely related to biotite monzonite granite, muscovite monzonite granite, and felsophyre, but the nature of granitic magma and its relationship with mineralization is relatively weak. In this paper, U-Pb dating, Lu-Hf isotope, the in situ composition of zircon, and the apatite of biotite monzonite granite, muscovite monzonite granite, and felsophyre in the Darongxi mining area are systematically studied, and the formation age, magma property and source, and their relationship with mineralization are discussed. The values of zircon U-Pb age and the $\epsilon_{\text{Hf}}(t)$ of biotite monzonite granite are 222.2 ± 0.54 Ma and $-2.9 \sim -6.4$, respectively. The values of zircon U-Pb age and the $\epsilon_{\text{Hf}}(t)$ of muscovite monzonite granite are 220.8 ± 0.58 Ma and -2.7 to -8.1 , respectively. The values of zircon U-Pb age and the $\epsilon_{\text{Hf}}(t)$ of felsophyre are 222.3 ± 2.20 Ma and $-2.2 \sim -5.4$, respectively. Magmatic apatite grains from biotite monzonite granite and muscovite monzonite granite show distinctive core-rim and oscillatory zoning textures in CL images, and demonstrate a bright yellow in colorful CL images. The magmatic apatite has a total rare earth concentration (3766–4627 ppm), exhibiting right-inclined nomalized rare earth element patterns and obvious negative Eu anomalies. The geochemical data of magmatic zircon and apatite indicate that magma sources are responsible for these intrusions in the Darongxi mining area, mainly derived from the partial melting of the Mesoproterozoic crust, which is rich in W; the magma is rich in F and poor in Cl ($F = 2.4 \sim 3.3$ wt%, $Cl = 0.0024 \sim 0.0502$ wt%). The oxygen fugacity of magmatic zircon ($\Delta\text{FMQ}_{\text{AVG}} = -4.02 \sim -0.26$), the high negative Eu anomaly ($\delta\text{Eu} = 0.06 \sim 0.12$) and the low positive Ce anomaly ($\delta\text{Ce} = 1.09 \sim 1.13$) of magmatic apatite, and the occurrence of ilmenite all indicate that the redox condition of magma from the Darongxi mining area is reduced. The reduced F-rich crust-source granitic rock and W-rich source provide favorable conditions for the mineralization of the Darongxi reduced skarn W deposit.



Citation: Cai, L.; Li, W.; Xie, G.; Yin, F. The Relationship between Granitic Magma and Mineralization in the Darongxi Skarn W Deposit, Xiangzhong District, South China: Constrained by Zircon and Apatite. *Minerals* **2024**, *14*, 280. <https://doi.org/10.3390/min14030280>

Academic Editor: Aleksei V. Travin

Received: 21 December 2023

Revised: 2 March 2024

Accepted: 5 March 2024

Published: 7 March 2024

Keywords: zircon; apatite; magma properties; Darongxi; skarn W deposit; Xiangzhong district



Copyright: © 2024 by the authors. Licensee MDPI, Basel, Switzerland. This article is an open access article distributed under the terms and conditions of the Creative Commons Attribution (CC BY) license (<https://creativecommons.org/licenses/by/4.0/>).

1. Introduction

Skarn deposit is one of the most important types of W deposit, accounting for more than 60% and 45% of the total W reserves in China and the world, respectively. Its mineralization is related to intermediate and felsic intrusive rocks [1]. The ore-bearing magma of the skarn W deposit can be either oxidized lowly fractioned diorite magma or reduced highly fractioned granitic magma [2]. The magma associated with skarn W deposits include S and I types, and the formation of most large-scale W deposits is mostly related to reduced S-type granitic rocks that mostly originate from the crust [3–5]. The formation of W-Mo and W-Mo-Cu deposits is related to I-type granodiorite from crust–mantle mixed sources [6,7]. For example, the Zhuxiling W-Mo deposit in China and the Salau W deposit in France are

associated with I-type granodiorite [8,9]. Studies have revealed that volatiles, such as F, can play an active role in the mineralization of magmatic hydrothermal deposits, which can increase the solubility of high field strength elements, reduce the minimum liquidus temperature of the system, change the fusible components of the granite melt, and promote the enrichment of W [10–12]. Therefore, it is the key to understand skarn W deposits in order to determine the nature and source of ore-bearing magma and the concentration of volatiles like F.

The Xiangzhong district is a unique Sb-Au-W metallogenic area, which is famous for the world's largest Xikuangshan Sb deposit and the most representative Woxi Au-Sb-W deposit [13,14]. Except for these deposits that formed from low-temperature fluids, several medium- and large-sized skarn and porphyry W deposits have been discovered in recent years, such as Darongxi, Muguayuan, and Caojiaba. The question of whether granites are S- or I-type has been the subject of discussion for a long time [15–17]. Relatively few studies focus on the volatiles and redox state of magmas. Zircon and apatite are common accessory minerals in magmatic rocks; they contain information regarding the magma, including crystallization age, temperature, oxygen fugacity, and volatiles, etc. [18–20]. The medium-sized Darongxi W deposit, located in the outer contact zone of the Dashenshan granite in the Late Triassic [21], develops multi-generation magma and is an ideal object for exploring the coupling relationship between magma and W mineralization.

In this paper, zircon from intrusions from the Darongxi deposit, including biotite monzonite granite, muscovite monzonite granite, and felsophyre, is studied through the use of trace element, U-Pb dating, and Lu-Hf isotope analysis. Apatite in biotite monzonite granite and muscovite monzonite granite were selected for BSE and CL petrographic identification and the analysis of major and trace elements. The purpose is to provide new constraints on the formation age, nature, and source of magma, and the mineralization of granite rocks in Darongxi deposit.

2. Geological Setting

2.1. Regional Geology

In the Neoproterozoic, the Jiangnan orogenic belt was formed by the convergence of the Yangtze plate and the Cathaysia Plate [22]. In the orogenic belt, Neoproterozoic metamorphic pyroclastic rocks and sedimentary rocks are mainly exposed, followed by meso-Cenozoic continental sedimentary rocks [23]. Since the Neoproterozoic, the Jiangnan orogenic belt has undergone multiple phases of magmatic activity and W mineralization [24,25], forming a world-class Jiangnan W polymetallic metallogenic belt [26].

The Xiangzhong district is located in the central-western part of Jiangnan orogenic belt (Figure 1a). The strata of the region are dominated by Neoproterozoic and Paleozoic strata, and the Neoproterozoic strata mainly include Slate and conglomerate, and the Paleozoic strata mainly include shale and sandstone. Magmatic rocks in the region are mainly Devonian and Triassic granite. Triassic granite occupy most magmatic rocks, and are distributed in a faceted pattern around the periphery of the Xiangzhong basin (Figure 1b). Most of them have the characteristics of multi-stage intrusion, and the lithology is mainly biotite granite and monzonitic granite. More than 170 Au, Sb, W metal associate deposits have been discovered [27–29]. According to geological characteristics, W deposits in this area can be divided into three types. The first type is skarn, which is represented by Darongxi and Caojiaba [21,30]. The second type is a porphyry W deposit, represented by Muguayuan [24]. The third type is a quartz vein W deposit, which is represented by Yangjiashan and Shaxi [31–33] (Table 1).

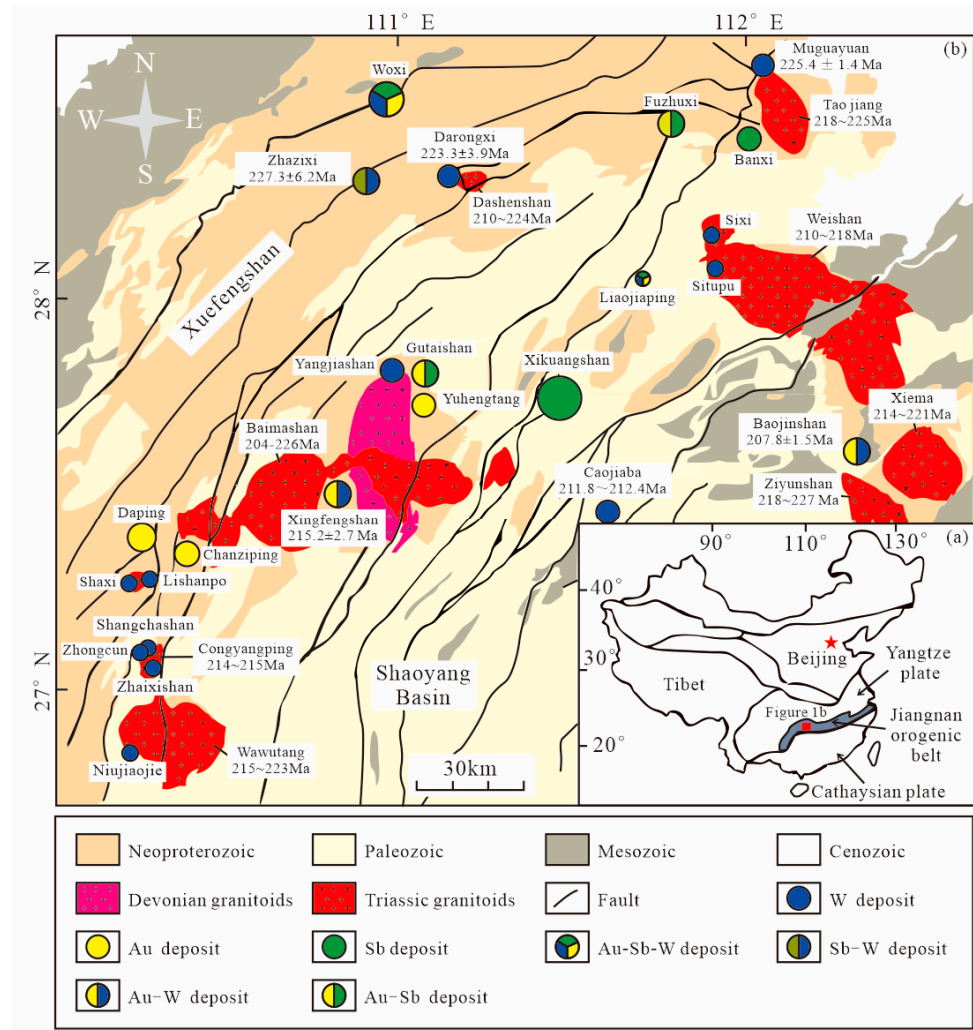


Figure 1. Geological map showing the location of the Xiangzhong district (a) and the distribution of magmatic rocks and related ore deposits (b) (modified after [32]); the detailed dating methods and references for the ages of the deposits and plutons in the figure are shown in Table 1.

Table 1. Statistical table of the age of W deposits and related pluton in Xiangzhong district.

Deposit	Deposit Age (Ma)	Uncertainty	Method of Dating	Reference	Related Pluton	Pluton Age (Ma)	Method of Dating	Uncertainty	Reference
Darongxi W deposit	223.3 ± 3.9	2σ	Molybdenite Re-Os	[34]	Dashenshan	210~224	Zircon U-Pb	1σ	[35,36]
						221~222	Zircon U-Pb	1σ	This study
Muguayuan W deposit	225.4 ± 1.4	2σ	Molybdenite Re-Os	[37]	Taojiang	218~225	Zircon U-Pb	1σ	[38]
Xingfengshan Au-W deposit	215.2 ± 2.7	1σ	Titanite U-Pb	[39]	Baimashan	204~226	Zircon U-Pb	1σ	[15]
Baojinshan Au-W deposit	207.8 ± 1.5	2σ	Scheelite Sm-Nd	[40]	Ziyunshan	218~227	Zircon U-Pb	1σ	[16]
Caojiaba W deposit	211.8~212.4	1σ	Wolframite U-Pb	[41]					
Zhazixi W deposit	227.3 ± 6.2	1σ	Scheelite Sm-Nd	[42]	Weishan	210~218	Zircon U-Pb	1σ	[17]
					Congyangping	214~215	Zircon U-Pb	1σ	[31]
					Wawutang	215~223	Zircon U-Pb	1σ	[43]
					Xiema	214~221	Zircon U-Pb	1σ	[44]

2.2. Deposit Geology

The Darongxi skarn W deposit average grade of $w(\text{WO}_3)$ is 0.49%, and the reserve is 40,000 tons. Four tungsten veins have been identified in the mining area; vein I is \ W-bearing skarn (Figures 2 and 3), and veins II, III, and IV are W-bearing quartz veins (Figure 3) [21]. Orebodies of a W-bearing skarn are distributed mainly within the manganese limestone and metamorphic sandstone of the lower member of the Nantuo Formation (Figure 3) [21]. The W-bearing skarn minerals are mainly pyroxene and garnet; the pyroxene is of the diopside-hedenbergite-schefferite series, and garnet is mainly grossular and almandine-spessartine [21]. Sulfides are mainly composed of pyrite, sphalerite, pyrrhotite, chalcopyrite, and minor molybdenite [21]. These minerals like hedenbergite, grossular and almandine-spessartine recognized Darongxi are reduced as skarn W deposits [21].

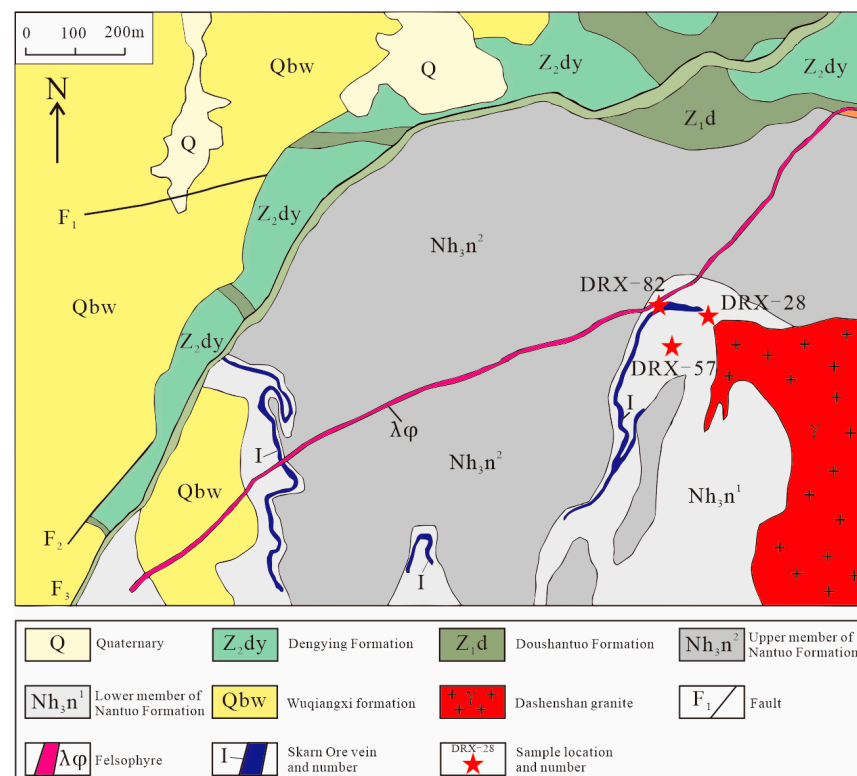


Figure 2. Geological map of the Darongxi W deposit (modify after [21]).

Three types of intrusive rocks are exposed in Darongxi, including biotite monzonite granite, muscovite monzonite granite, and felsophyre.

- (1) Grayish white medium-coarse-grained biotite monzonite granite, with granitic texture (Figure 4a). Fine quartz veins and aplite veins can be seen locally, and garnetization and chloritization are locally developed, and the alteration width is about 10~15 cm (Figure 4b). The main minerals include orthoclase (20%–25%), plagioclase (25%–30%), quartz (30%–40%). The minor minerals are muscovite (1%–5%), biotite (5%–10%), albite (1%–5%), and chlorite (1%–5%). The accessory minerals are mainly grossular, zircon, almandine-spessartine, and apatite (Figure 5a–e), and some biotite was altered into muscovite and chlorite (Figure 5f).
- (2) Medium-fine-grained muscovite monzonite granite with granitic texture, which mainly intrudes into the slate of the Nantuo Formation in the form of veins (Figure 4c), the width is about 5~20 cm, and a large amount of muscovite can be seen locally. The main minerals include quartz (40%–45%) and orthoclase (30%–35%), while the minor minerals are plagioclase (5%–10%), albite (5%–10%), biotite (1%–5%), and muscovite (1%–5%). The accessory minerals are ilmenite, almandine-spessartine, apatite, chlo-

- rite, schorl, zircon (Figure 5g–j). Some biotite are altered into muscovite and chlorite (Figure 5k).
- (3) Felsophyre is light yellowish brown and mainly intrudes into the Nantuo Formation in the form of veins (Figure 4d). The veins are wide, about 3 m, with porphyritic structures. The phenocryst is mainly quartz (50%–60%), albite (15%–20%), orthoclase (15%–20%), and muscovite (10%–15%). Several quartz veins crosscutting felsophyre can be seen (Figure 5l).

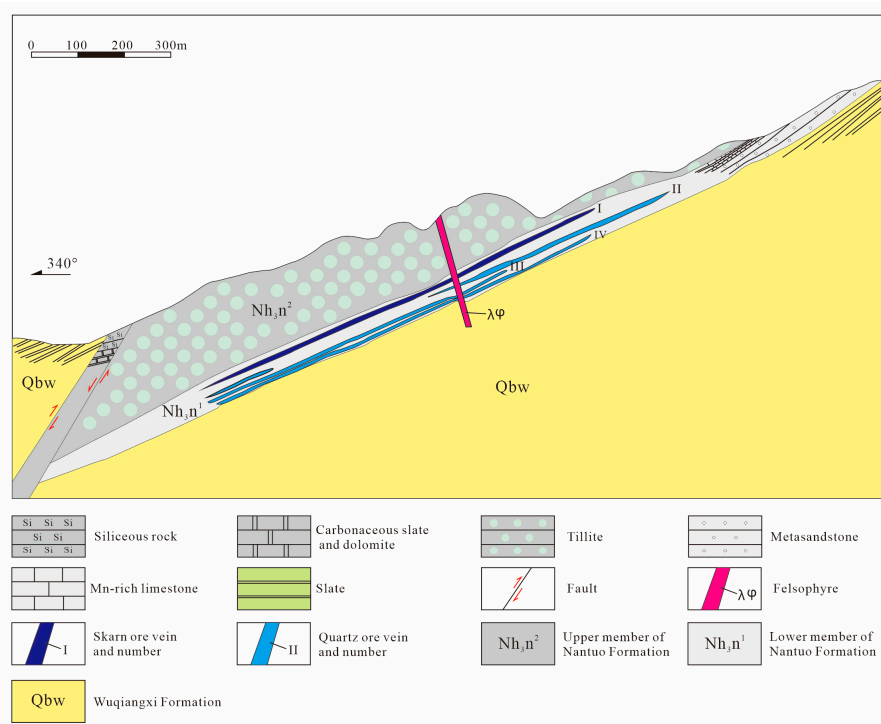


Figure 3. Geological section of the Darongxi tungsten deposit (modify after [21]).

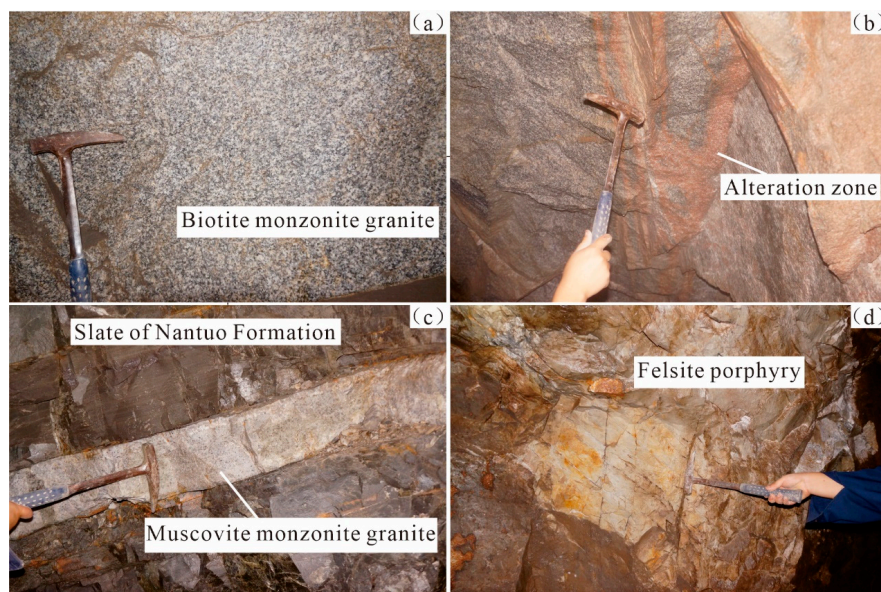


Figure 4. Photographs of granitic rock in the Darongxi mining area. (a) Biotite monzonite granite; (b) biotite monzonite granite having undergone garnet and chlorite alteration; (c) muscovite monzonite granite; (d) felsophyre.

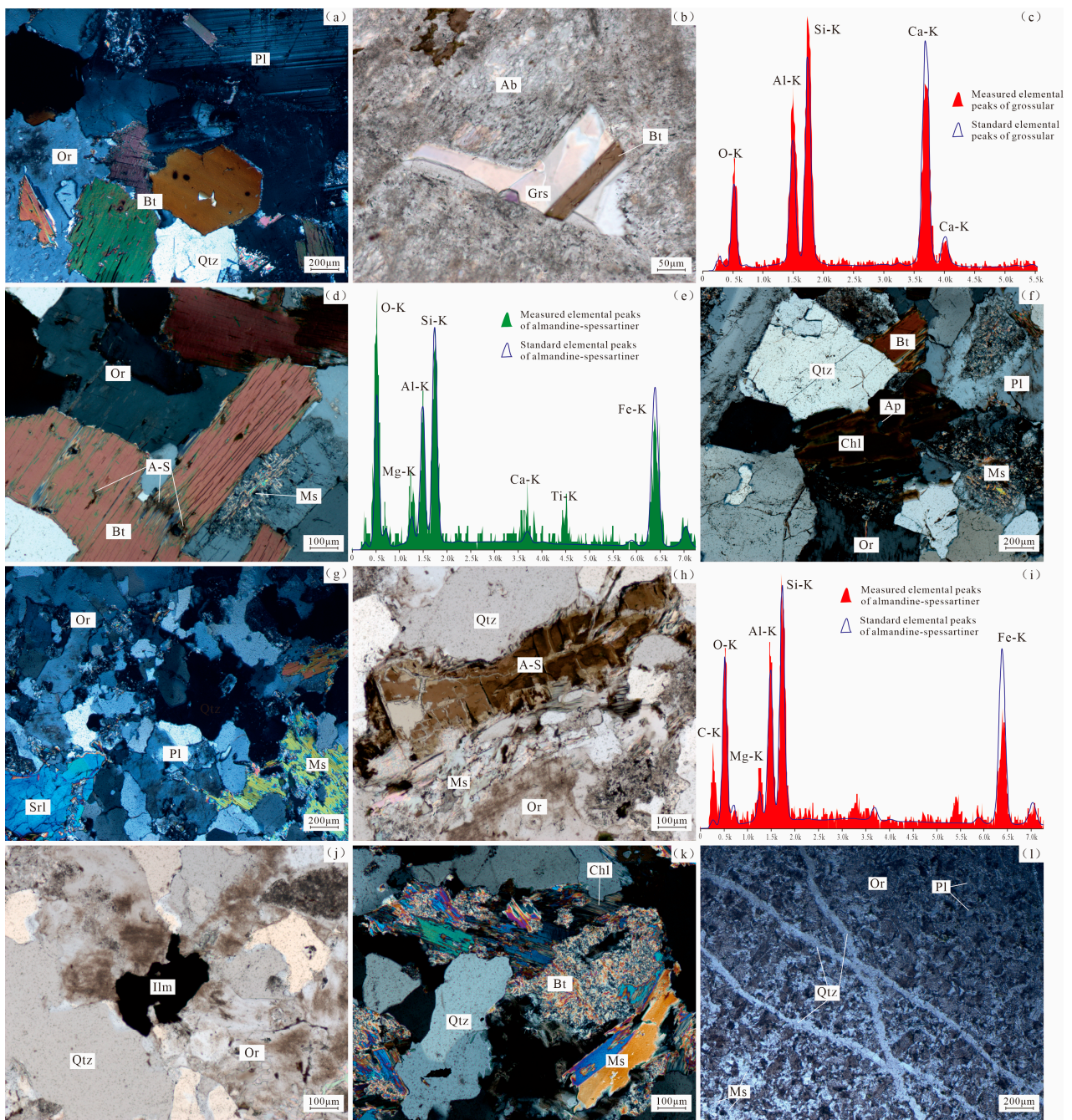


Figure 5. Photomicrograph of granitic rock in the Darongxi mining area. (a) Photomicrograph of biotite monzonite granite; (b) grossular photomicrograph of biotite monzonite granite; (c) grossular elemental peak map of TIMA in biotite monzonite granite; (d) almandine-spessartine photomicrograph of biotite monzonite granite; (e) almandine-spessartine elemental peak map of TIMA in biotite monzonite granite; (f) photomicrograph of biotite monzonite granite chlorite and muscovite alteration; (g) photomicrograph of muscovite monzonite granite; (h) almandine-spessartine photomicrograph of muscovite monzonite granite; (i) almandine-spessartine elemental peak map of TIMA in muscovite monzonite granite; (j) ilmenite photomicrograph of muscovite monzonite granite; (k) photomicrograph of muscovite monzonite granite chlorite and muscovite alteration; (l) photomicrograph of felsophyre. (a,d,f,g,k)—Crossed polarized light; (b,h,j,l)—Plane polarized light. Abbreviations: A-S = almandine-spessartine; Qtz = quartz; Ap = apatite; Bt = biotite; Srl = schorl; Chl = chlorite; Ms = muscovite; Ab = albite; Grs = grossular; Pl = plagioclase; Ilm = ilmenite; Or = orthoclase.

The magmatic apatite from biotite monzonite granite (Ap_{m-B}) and muscovite monzonite granite (Ap_{m-M}) have similar petrographic characteristics, and mainly occur as inclusions in biotite, orthoclase, plagioclase, and quartz (Figure 6a,e). These apatite grains are mainly euhedral–subhedral short or long columns, with sizes ranging from 30 to 60 μm . In the BSE image, they are mostly homogeneous in texture, and some show core–rim and zoning textures (Figure 6c). In the colorful CL image, the magmatic apatite (Ap_m) is bright yellow (Figure 6d,f).

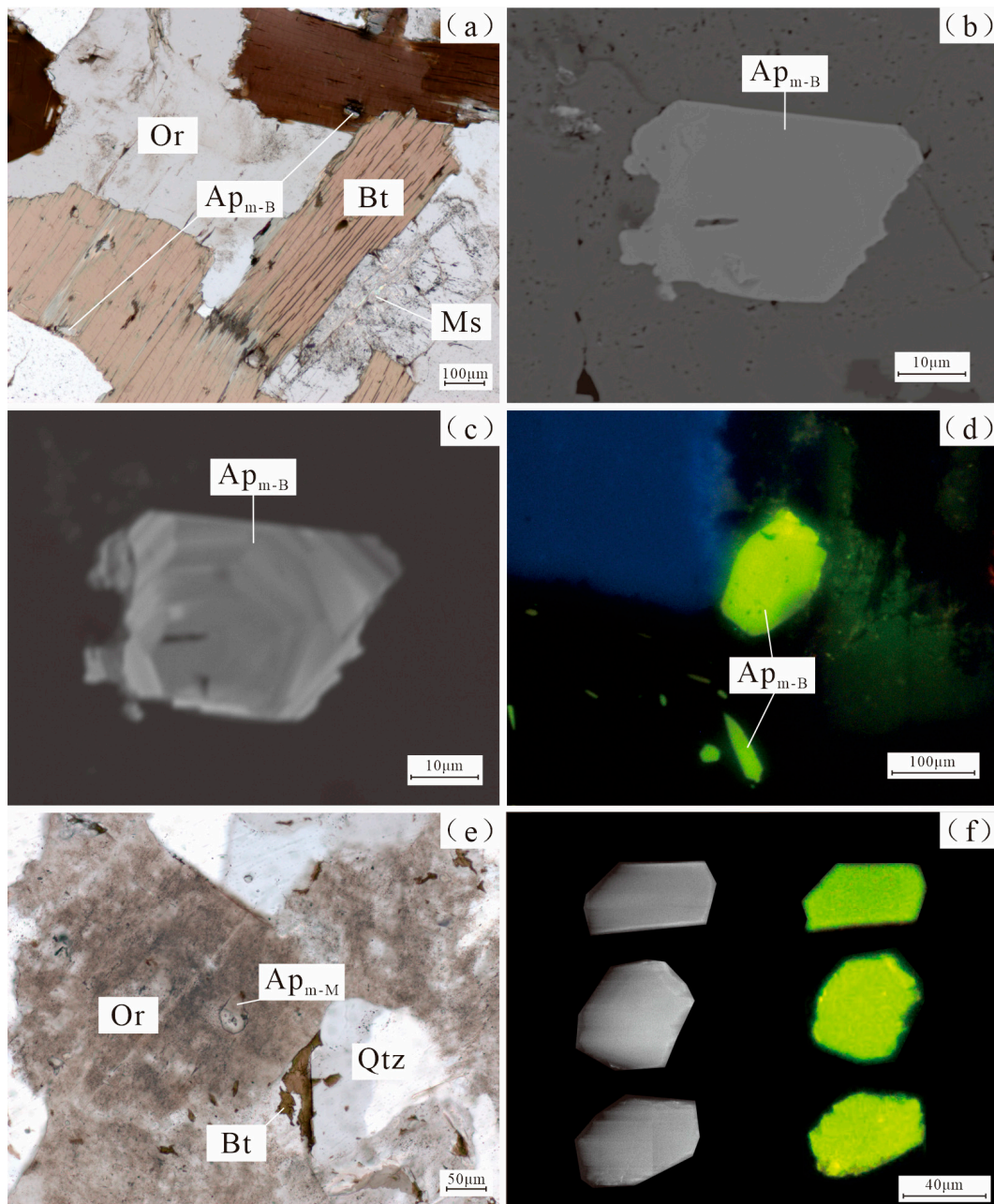


Figure 6. Lithographic photos of granite magmatic apatite in the Darongxi mining area. (a) Photomicrograph of biotite monzonite granite magmatic apatite; (b) BSE image of biotite monzonite granite magmatic apatite; (c) CL image of biotite monzonite granite magmatic apatite; (d) colorful CL image of biotite monzonite granite magmatic apatite; (e) photomicrograph of muscovite monzonite granite magmatic apatite; (f) BSE and colorful CL images of muscovite monzonite granite magmatic apatite. Abbreviations: Qtz = quartz; Or = orthoclase; Bt = biotite; MS = muscovite.

3. Sampling and Analytical Methods

The samples involved were collected in the mining district. The DRX-28 biotite monzonite granite, part of the Dashenshan granite, was collected from the 290 m adit of the eastern part of the Darongxi mining area. Muscovite monzonite granite was collected from the 20 m adit of the eastern part of the Darongxi mining area. DRX-82 felsophyre was collected from the 440 m adit of the eastern part of the Darongxi mining area. The sample location is shown in Figure 2. The analyzed zircon of the three types of rocks and apatite of muscovite monzonite granite are separated from the host sample. The apatite of the biotite monzonite granite was analyzed in the thin sample section. The integrated mineral automatic analysis of the mineral composition of intrusive rocks and mineral CL image shooting were completed in the TIMA Laboratory, Key Laboratory of Strategic Metal Mineral Prospecting Theory and Technology Department, Ministry of Natural Resources, China University of Geosciences (Beijing, China). The analysis instrument was automatic mineral analysis system of the TESCAN Electron Microscope Company (Shanghai, China). The instrument model was the TIMA-GMS. The sample to be tested was carbonized before the experiment, and the sample to be tested was glued to the sample table with conductive adhesive. In the vacuum mode, the working distance was adjusted to 15 mm, the acceleration voltage was adjusted to 25 keV, the current was adjusted to 10 nA, the platinum Faraday cup automatic program was used for the calibration of the current and BSE signal strength, and the Mn standard sample was used for the calibration of the EDS signal. In the test, a lattice pattern of the dissociation-mode analysis was used to obtain both EDS data and BSE images, with an X-ray count of 1500 kcps at each point. The field length was 1000 μm , the pixel size was 3 μm , and the energy spectrum step was 9 μeV . The CL image experimental probe was a telescopic panchromatic CL detector (standard Edition) with a wavelength range of 185–850 nm (ultraviolet light, visible light, and near infrared light). In the vacuum mode, the acceleration voltage was set to 10 keV, the current was set to 300 pA, the beam spot size was 5 nm, and the working distance was 15 mm. The ambient conditions include a temperature of 22 °C and 45% humidity.

The zircon trace element concentration and U-Pb dating were completed using LA-ICP-MS analysis at the Yanduzhongshi Geological Analysis Laboratories Ltd. (Beijing, China). The laser-ablation system was the NWR193 laser-ablation microprobe (Elemental Scientific Lasers LLC) (Shanghai, China), and the ICP-MS Instrument was the Analytikjena PlasmaQuant MS quadrupole ICP-MS. Zircon trace element and U-Pb dating were carried out in situ using the above instruments. During the laser ablation process, the carrier gas was helium and the compensation gas was argon gas. These were mixed using a Y-shaped junction before entering ICP to adjust the sensitivity. Approximately a 20–30 s blank signal and a 40 s sample signal were included in every time-resolved analysis. U-Th-Pb isotope ratios and ages, the calculation for elemental concentrations, the drift correction of instrument sensitivity, the selection of samples and blank signals, and other offline processing of data was completed using software ZSkits (ZSkits 1.1.0, Yanduzhongshi Geological Analysis Laboratory Ltd., Beijing, China). The 91500 zircon was used as a primary standard [45], Plešovice and Tanz are used as secondary standards [46]. The zircon trace element was quantitatively calculated using SRM610 as the external standard and Si as the internal standard. A standard-sample bracketing method was used to correct the fractionation of the U-Pb ratio, mass bias, and instrument drift. For quality control, we insert zircon standards like Plesovice and Tanz between every 10 unknown samples. Isoplot 4.15 [47] was used to calculate the weighted average ages and plot the concordia diagram. The testing denuded diameter of zircons and standards was 25 μm . All standard sample Tanz [48], Plesovice [46], and 91500 [45] coincide with the recommended values. The weighted average mean of Plesovice and Tanz are 337.0 ± 1.7 (2 s, MSWD = 0.22, n = 10) and 568.0 ± 2.9 (2 s, MSWD = 0.23, n = 10), respectively. The uncertainty level of zircon U-Pb dating was 1-sigma, as shown in the Supplementary Table S2. The detailed analysis conditions are shown in the Supplementary Table S1 Analysis conditions.

Zircon Hf isotope analysis was carried out at the MNR Key Laboratory of Metallogeny and Mineral Assessment, Institute of Mineral Resources, Chinese Academy of Geological Sciences, Beijing, China. The laser-ablation system is the Resolution S155 laser-ablation microprobe, and the ICP-MS instrument is the Neptune multi-collector ICP-MS. All Hf isotope-measured spots are selected from the position for in situ U-Pb analyses. Depending on the size of the ablation domain, the beam diameter was chosen to be 40 or 55 μm , and fixed points were used for this analysis. In a mixing chamber mixed with argon, the ablated sample was transported from the laser-ablation cell to the ICP-MS torch using helium as a carrier gas. The determination of $^{176}\text{Lu}/^{175}\text{Lu} = 0.02658$ and $^{176}\text{Yb}/^{173}\text{Yb} = 0.796218$ ratios is helpful to correct the isobaric interferences of ^{176}Lu and ^{176}Yb on ^{176}Hf [49]. In order to correct the instrumental mass bias, exponential law was used to normalize the Yb isotope ratios, with $^{172}\text{Yb}/^{173}\text{Yb}$ being 1.35274 [49], and the Hf isotope ratios with $^{179}\text{Hf}/^{177}\text{Hf}$ being 0.7325. Studies [50,51] have described the detailed mass bias correction protocols, and we assumed the mass bias behavior of Lu followed that of Yb. During analysis, the reference standards are Zircon GJ1 and a high Yb synthetic zircon Zr5, with a weighted mean $^{176}\text{Hf}/^{177}\text{Hf}$ ratio of 0.282007 ± 0.000007 (2σ , $n = 36$) and 0.282212 ± 0.000015 (2σ , $n = 3$). The solution analysis, inspired by [49,52], was used to calculate the weighted mean $^{176}\text{Hf}/^{177}\text{Hf}$ ratio of 0.282000 ± 0.000005 (2σ) and 0.282202 ± 0.000006 (2σ), and they are not distinguishable. The uncertainty level of the zircon Lu-Hf isotope is 2-sigma, as shown in the Supplementary Table S3. The detailed analysis conditions are shown in the Supplementary Table S1 Analysis conditions.

The apatite major element was completed in situ using an electron probe microanalyzer in the Wuhan Sample Solution Analytical Technology Co., Ltd., Wuhan, China. The instrument was JXA-8230 of JEOL, the current was 10 nA, and the voltage was 20 KV. The peak analysis time of the K, Ca, Ti, La, Ce, Na, Mg, Al, Si, Sr, Nd, Pr, Mn, Fe, F, Cl, S, Zr, P, and Y elements was 10 s and the background analysis time was 5 s. Fifteen kinds of rare earth element standard samples, forty-four kinds of elemental standard samples, and fifty-three kinds of mineral standard samples provided by SPI company were used as the calibration standards. The ZAF correction method of JEOL was used for data correction. The detailed analysis conditions are shown in the Supplementary Table S1 Analysis conditions.

The apatite trace element was conducted using LA-ICP-MS at the Wuhan Sample Solution Analytical Technology Co., Ltd., Wuhan, China. The COMPexPro 102 ArF excimer laser, a MicroLas optical system, and a “wire” signal smoothing device [53] were included in the GeolasPro laser-ablation system. The ICP-MS instrument was Agilent 7900, and this can acquire ion-signal intensities. Helium was applied as a carrier gas. During the laser-ablation process, the carrier gas was helium and the compensation gas was argon gas. These were mixed using a Y-shaped junction before entering ICP to adjust the sensitivity. The spot size was 32 μm and the frequency was 5Hz. The NIST610 was used as the primary standard, and the four standards (BCR-2G, BHVO-2G, BIR-1G, and GSE-1G) were used as secondary standards [54]. Furthermore, the Na_2O , MgO , Al_2O_3 , P_2O_5 , K_2O , CaO , TiO_2 , MnO , and FeO were measured as internal standards. During each analysis, a background acquisition was taken after 20–30 s, and then data acquisition was taken from the sample after about 50 s. The quantitative calibration for trace element analysis, the time–drift correction, the integration of background and analyzed signals, and the performance of the offline selection was handled by ICPMSDataCal, which was based on Excel [54]. The uncertainty level of the apatite trace element is 1-sigma, as shown in the Supplementary Table S6. The detailed analysis conditions are shown in the Supplementary Table S1 Analysis conditions.

4. Results

4.1. Zircon U-Pb Dating

The LA-ICP-MS zircon U-Pb dating results are shown in the Supplementary Table S2. Biotite monzonite granite zircons are mostly shaped as long and short columns, while a few are irregular. The long axes ranged from 100 to 200 μm , the short axes ranged from 50 to

100 μm , and the length/width ratio was about 1:1 to 2:1. The Th/U ratio of zircon ranged from 0.23 to 0.67, with an average of 0.37. The Th and U concentrations are positively correlated, comparable to that of typical magmatic zircon. A total of twenty zircon U-Pb spots were tested for biotite monzonite granite, and seven spots had large errors and were therefore rejected. The remaining thirteen spots showed good community characteristics, and all of these were on or near the age concordance curve with concordances > 98%. The age concordance was 222.2 ± 0.54 Ma (MSWD = 0.15) (Figure 7a,b).

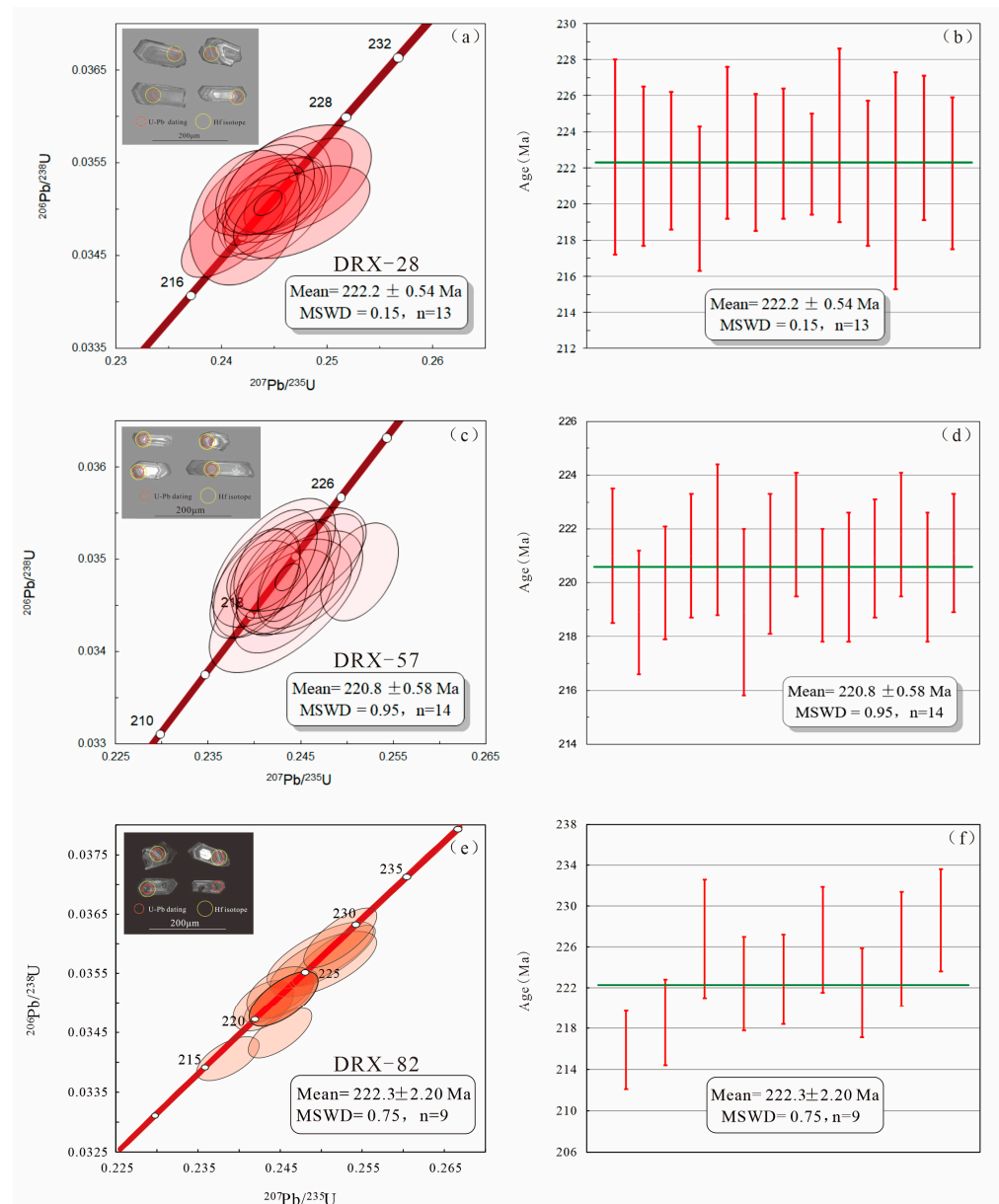


Figure 7. Cathodoluminescence images of representative zircon, Zircon U-Pb concordia diagrams, and the weighted mean ages of granitic rock in the Darongxi mining area. (a) Cathodoluminescence images of representative zircon, Zircon U-Pb concordia diagram of DRX-28; (b) the weighted mean ages diagram of DRX-28; (c) Cathodoluminescence images of representative zircon, Zircon U-Pb concordia diagram of DRX-57; (d) the weighted mean ages diagram of DRX-57; (e) Cathodoluminescence images of representative zircon, Zircon U-Pb concordia diagram of DRX-82; (f) the weighted mean ages diagram of DRX-82. The red line in (b,d,f) represents the error bar for each test point, and the green line represents the weighted average age.

Zircons from muscovite monzonite granite are usually long and short column shaped, with the long axes ranging from 100 to 180 μm , the short axes ranging from 50 to 80 μm , and the length/width ratio being about 1:1 to 2:1. The Th/U ratio of zircon ranges from 0.24 to 0.32, with an average of 0.25. A total of twenty zircon U-Pb spots were tested for muscovite monzonite granite, among which, six spots had large errors and were not used. The remaining fourteen spots showed good community characteristics, and the spots fell on the age concordance curve with concordances > 97%, and concordant ages of 220.8 ± 0.58 Ma (MSWD = 0.95) (Figure 7c,d).

Zircons from felsophyre are again long and short columns, with a few being irregular, with the long axes ranging from 50 to 200 μm , the short axes ranging from 50 to 90 μm , and the length/width ratio being about 1:1 to 2:1. Some zircons have complex internal structures, which may have been subjected to late hydrothermal alterations. A total of 30 zircon U-Pb spots were tested on the site. Eight spots had low concordances and thirteen spots had large errors; these were rejected. The remaining nine spots showed good community characteristics. The spots fell on the age concordance curve with concordances > 99%, and the concordance was 222.3 ± 2.20 Ma (MSWD = 0.75) (Figure 7e,f).

4.2. Lu-Hf Isotope Data for Zircon

The zircon Hf isotope analyzing results are shown in the Supplementary Table S3. All Hf isotope measured spots were selected from the position for in situ U-Pb analyses, and the representative spots are shown in Figure 7a. A total of 14 grains were analyzed, and they yield uniform Hf isotope compositions, with the $^{176}\text{Hf}/^{177}\text{Hf}$ ratio ranging from 0.2825 to 0.2826 (an average of 0.2825). $\epsilon_{\text{Hf}}(t)$ are all negative values, ranging from -6.4 to -2.9 , with an average of -4.9 . The two-stage model ages ($T_{2\text{DM}}$) range from 1436 Ma to 1653 Ma, with an average of 1563 Ma.

All Hf isotope measured spots were selected from the position for in situ U-Pb analyses, and the representative spots are shown (Figure 7c). A total of 13 grains were analyzed. The Hf isotope compositions of these were uniform, and the $^{176}\text{Hf}/^{177}\text{Hf}$ ratio ranged from 0.2824 to 0.2826, with an average of 0.2825. $\epsilon_{\text{Hf}}(t)$ are all negative, ranging from -8.1 to -2.7 , with an average of -5.2 . The $T_{2\text{DM}}$ ranged from 1420 Ma to 1761 Ma, with an average of 1577 Ma.

All Hf isotope measured spots were selected from the position for in situ U-Pb analyses, and the representative spots are shown (Figure 7e). A total of seven grains were analyzed. The Hf isotope compositions were uniform, and the $^{176}\text{Hf}/^{177}\text{Hf}$ ratio ranged from 0.2825 to 0.2826, with an average of 0.2825. $\epsilon_{\text{Hf}}(t)$ are all negative, ranging from -5.4 to -2.2 , with an average of -3.7 . The $T_{2\text{DM}}$ ranged from 1398 Ma to 1595 Ma, with an average of 1486 Ma.

4.3. The Trace Element Composition of Zircon

The zircon trace element analytical results are shown in the Supplementary Table S4. The Ti concentrations of zircon from biotite monzonite granite ranged from 1.4 ppm to 7.8 ppm, with an average of 4.5 ppm. The total of the rare earth elements (ΣREE) ranged from 825 ppm to 1610 ppm, with an average of 1148 ppm. The LREE were depleted and the HREE were enriched, the LREE/HREE was 0.01~0.05, with the average being 0.02. There are some positive Ce anomalies and negative Eu anomalies. δCe ranged from 4.0 to 82.1, with an average of 36.2. δEu ranged from 0.13 to 0.46, with an average of 0.22 (Figure 8a).

Th titanium concentrations of zircon from muscovite monzonite granite ranged from 1.5 ppm to 11.5 ppm, with an average of 6.3 ppm. The ΣREE ranged from 1064 ppm to 1551 ppm, with an average of 1240 ppm. LREE were depleted and HREE were enriched, and the LREE/HREE ranged from 0.01 to 0.04, with an average of 0.02. There are some positive Ce anomalies and negative Eu anomalies, with δCe ranging from 12.5 to 47.6, with an average of 28.4, and δEu ranging from 0.16 to 0.30, with an average of 0.24 (Figure 8b).

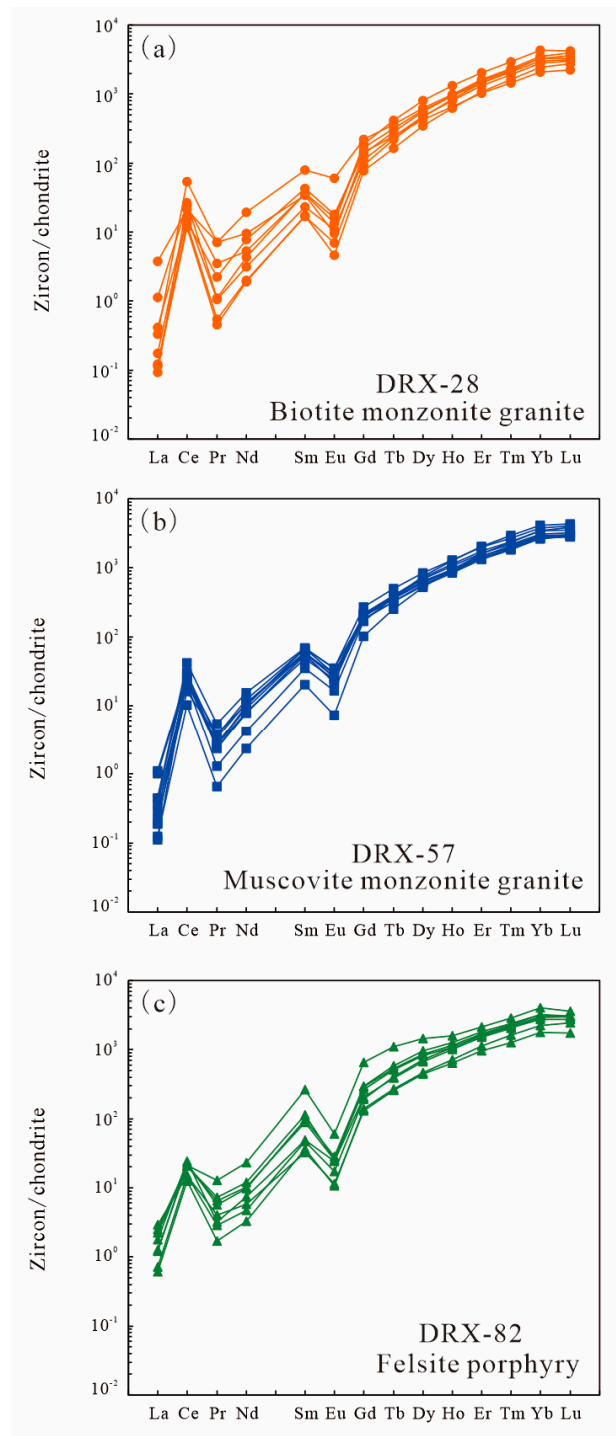


Figure 8. Chondrite-normalized REE patterns of zircon in the granitic rock of the Darongxi mining area. Data for the chondrite are from [55]. (a) Chondrite-normalized REE patterns of zircons in biotite monzonite granite (DRX-28); (b) Chondrite-normalized REE patterns of zircons in muscovite monzonite granite (DRX-57); (c) Chondrite-normalized REE patterns of zircons in felsophyre (DRX-82).

The titanium concentrations of zircon from felsophyre zircon range from 5.0 ppm to 24.2 ppm, with an average of 9.5 ppm. The Σ REE were 738 ppm~1895 ppm, with an average of 1242 ppm. LREE were depleted and HREE were enriched, and the LREE/HREE ranged from 0.02 to 0.04, with an average of 0.03. There are some positive Ce anomalies

and negative Eu anomalies. δCe ranged from 3.7 to 12.4, with an average of 7.7, and δEu ranged from 0.14 to 0.24, with an average of 0.17 (Figure 8c).

4.4. Major and Trace Element Composition of Apatite

The major element concentrations of apatite from biotite monzonite granite and muscovite monzonite granite show no significant differences (CaO: $\text{Ap}_m\text{-B}$: AVG = 55.39 wt%, $\text{Ap}_m\text{-M}$: AVG = 55.37 wt%; P_2O_5 : $\text{Ap}_m\text{-B}$: AVG = 42.23 wt%, $\text{Ap}_m\text{-M}$: AVG = 41.51 wt%; F: $\text{Ap}_m\text{-B}$: AVG = 2.76 wt%, $\text{Ap}_m\text{-M}$: AVG = 2.74 wt%), and the rest of the oxides are mostly close to or below the detection limit, as shown in the Supplementary Table S5.

The analysis results of the trace elements in apatite are shown in the Supplementary Table S6. The trace element concentrations of the apatite from the biotite monzonite granite and the muscovite monzonite granite are broadly similar, with the overall pattern being mainly inclined to the right (Figure 9). The ΣREE in the magmatic apatite were high, and they ranged from 3766 to 4627 ppm, with an average of 4128 ppm. Magmatic apatite had high negative Eu anomalies, and δEu ranged from 0.06 to 0.12, with an average of 0.09. δCe ranged from 1.09 to 1.13, with an average of 1.12. La_N/Yb_N ranged from 1.8~6.1, with an average of 3.5. The differentiation of light and heavy rare earth is strong, with the $\text{LREE}/\text{HREE} = 2.1\sim 5.2$, with an average of 3.6.

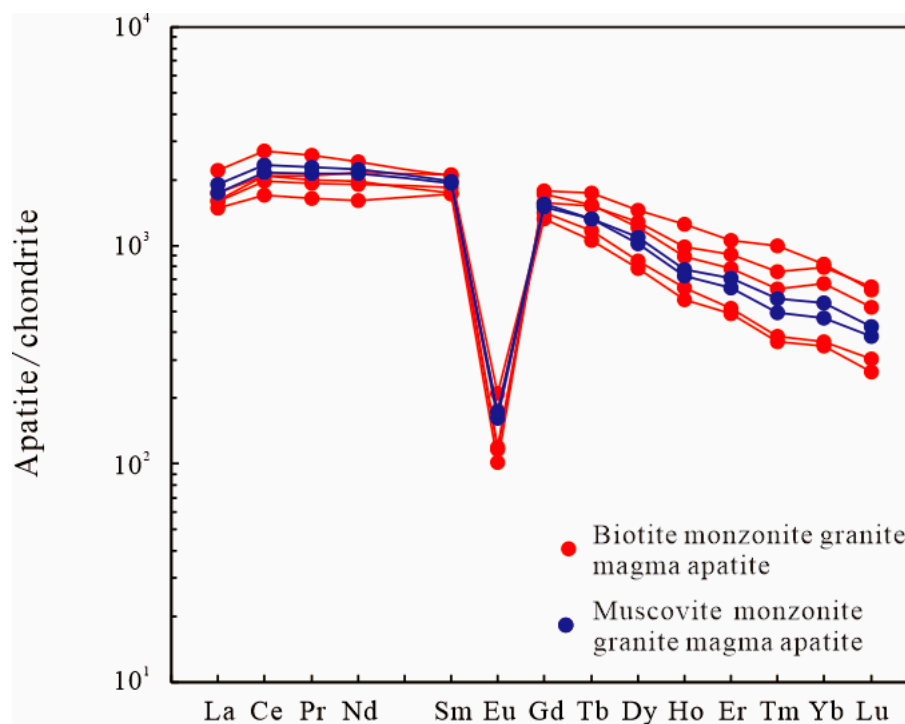


Figure 9. Chondrite-normalized REE patterns of apatite in the granite of Darongxi mining area. Data for the chondrite are from [55].

5. Discussion

5.1. Temporal and Spatial Distribution of W Deposits

In this paper, we obtained that biotite monzonite granite, muscovite monzonite granite, and felsophyre from the Darongxi mining area were formed between 220.8 and 222.3 Ma. These ages are similar to the age of the biotite monzonite granite comprising the adjacent Dashenshan granite (210~220 Ma [34,35]), indicating a close genetic relationship with the magmatic activity in the mining area and the Dashenshan pluton. These ages are consistent with the mineralization age of the Darongxi W skarn deposit, as the published molybdenite Re-Os age is 223.3 ± 3.9 Ma [36]. A large number of Au, Sb, and W deposits were formed in the Xiangzhong district, and most of the W deposits were formed near and inside magmatic rocks (Figure 1, Table 1). The Muguayuan porphyry W deposit was formed at

225.4 ± 1.4 Ma [37], which is similar to the surrounding Taojiang pluton (218 ± 3 Ma and 225 ± 3 Ma [38]). The Xingfengshan Au-W deposit was formed at 215.2 ± 2.7 Ma [39], which is similar in age to the surrounding Baimashan pluton (204–226 Ma [15]). The Baojinshan Au-W deposit was formed at 207.8 ± 1.5 Ma [40], which is similar in age to the surrounding Ziyunshan pluton (218–227 Ma [16]). In addition, the U-Pb age of wolframite in the Caojiaba W skarn deposit is 211.8–212.4 Ma [41], which was interpreted to be a distal reduced skarn W deposit genetically related to the concealed intrusion [30].

The Hf Isotope composition of granitic rock in the Darongxi mining area is uniform, and the $\epsilon_{\text{Hf}}(t)$ values of the three samples range from −8.1 to −2.2. In the $\epsilon_{\text{Hf}}(t)$ - t diagram (Figure 10), the three samples fall between the 1.8 Ga crust and the chondrite, which belongs to the juvenile crust, implying that its magma source mainly comes from the crust. The $T_{2\text{DM}}$ of the three samples ranged from 1398 to 1761 Ma, with an average of 1552 Ma, indicating that the crust source may be Mesoproterozoic juvenile crust. The Hf isotope results are similar to those of the Dashenshan pluton (Figure 10), which may be the product of homologous magmatic evolution. In this paper, the Hf isotope of granitic rocks in the Darongxi mining area is compared with that of Indosinian magmatic rocks in the Xiangzhong district, and the compiled results of the Hf isotope are similar, with $\epsilon_{\text{Hf}}(t)$ mostly ranging from 0 to −10. This indicates that the magmatic source of the Indosinian magmatic rocks in the Xiangzhong district is mainly a crust source, and may include a small amount of mantle. The $T_{2\text{DM}}$ is between 1000 and 2000 Ma, indicating that the crust source is mainly from the middle and late Proterozoic crust.

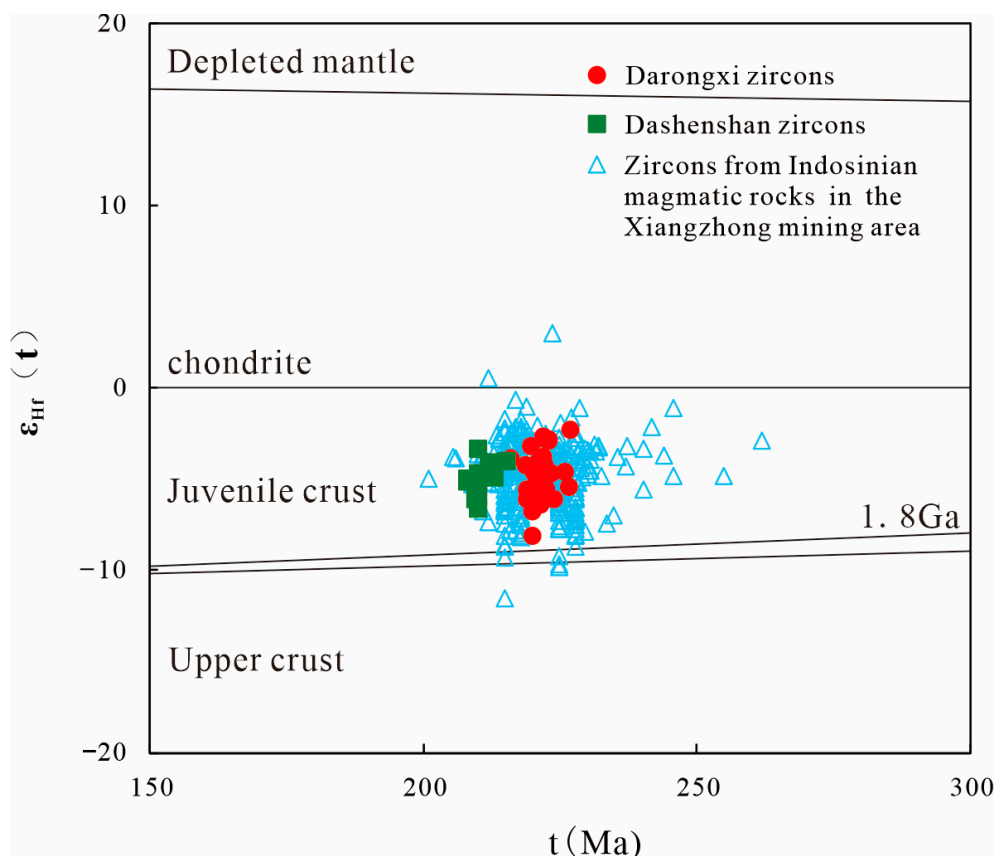


Figure 10. Zircon Hf isotope diagram of Indosinian magmatic rocks in the Xiangzhong district. Hf isotope data of the Dashenshan pluton are from [34], and Hf isotope data of Indosinian magmatic rocks are from [15–17,44,56,57].

5.2. The Nature of Ore-Bearing Magma

The titanium concentrations of zircon are strongly correlated with temperature [58]. The zircon Ti thermometer can be used to estimate its crystallization temperature, and thus

predict the crystallization temperature of magma. According to the calculation method of the zircon Ti thermometer [19], the magmatic rocks in the Darongxi mining area belong to felsic rocks, and zircon and quartz coexist in the silicon-saturated felsic rocks, therefore, we can assume that the SiO_2 activity is 1.0. Due to the absence of rutile, we assume the TiO_2 activity is 0.6 [19]. Based on the zircon Ti temperature calculation results, biotite monzonite granite was formed between 623.7 °C and 770.5 °C, with the weighted average value being 707.3 ± 3.1 °C. Muscovite monzonite granite was formed between 629.9 °C and 810.9 °C, and the weighted average was 736.4 ± 2.7 °C. Felsophyre was formed between 729.6 °C and 809.9 °C, with the weighted average value was 781.0 ± 1.9 °C. These relatively large variations in temperature for the granitic rocks in Darongxi indicate that the magma may have undergone a separation crystallization process [59].

There are two valence states of Ce in zircon, and oxidized Ce^{4+} is easier to replace Zr^{4+} than Ce^{3+} , which is reduced in a redox state. This makes the Ce anomaly of zircon the stronger choice for the evaluation of the redox state of magma [20]. In Darongxi granitic rocks, the zircon trace element concentrations of La and Ti are below 1 ppm and 50 ppm, respectively, thus eliminating the contamination of REE carrier mineral inclusions, iron-titanium oxides, fluid inclusions, and cracks in zircon [60,61]. By using the zircon oxygen fugacity calculation formula of [62,63], the $\lg(\text{fo}_2)$ of biotite monzonite granite ranged from -31.09 to -11.9 , with an average of -18.86 . The relative oxygen fugacity (ΔFMQ) ranged from -12.12 to 3.23 , with an average of -2.37 . The $\lg(\text{fo}_2)$ of muscovite monzonite granite ranged from -20.93 to -10.64 , with an average of -16.26 . ΔFMQ ranged from -3.15 to 3.76 , with an average of -0.26 . The $\lg(\text{fo}_2)$ of felsophyre ranged from -21.37 to -16.11 , with an average of -18.96 . ΔFMQ ranged from -6.19 to -1.83 , with an average of -4.02 . In the zircon $\lg(\text{fo}_2)-10^4/T$ and $\delta\text{Ce}-10^4/T$ diagrams (Figure 11), only a few samples were above the FMQ, while most zircons are below the FMQ, and the overall oxygen fugacity is lower than that of the FMQ buffers, indicating that magma in the Darongxi mining area is of a low oxygen fugacity.

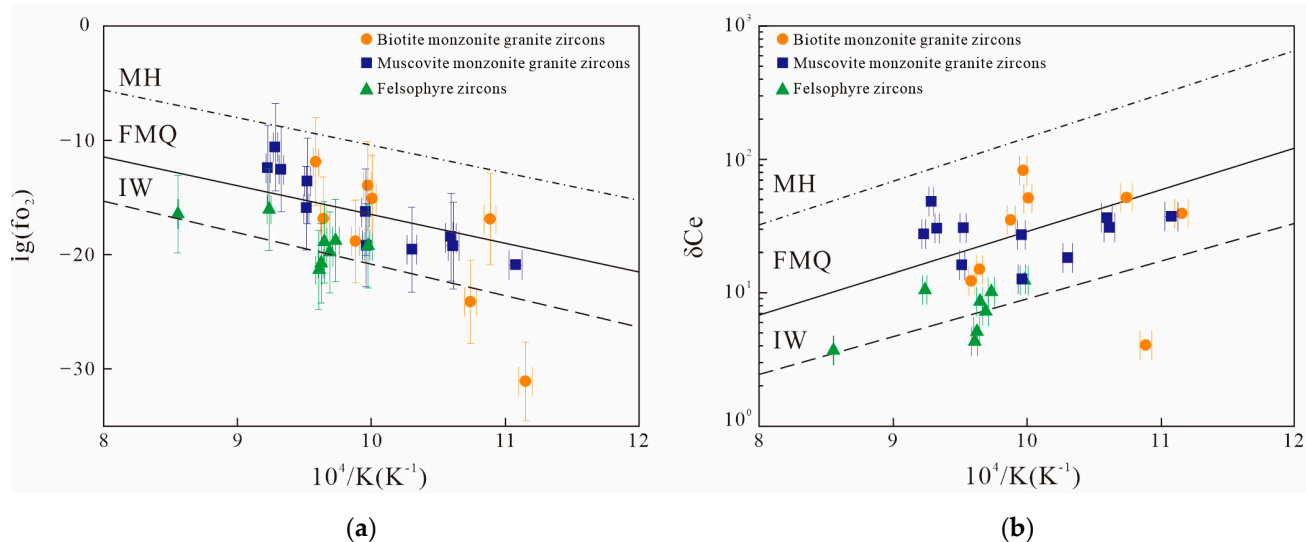


Figure 11. Zircon diagram of (a) $\lg(\text{fo}_2)-10^4/T$ and (b) $\delta\text{Ce}-10^4/T$. Map a is from [62]. Map b is from [63]; FMQ: Fayalite-Magnetite-Quartz buffer; MH: Magnetite-Hematite; IW: Iron-Wustite buffer. $K = T_{\text{Zr}} + 273.15$. T_{Zr} is zircon Ti thermometer.

The $\text{Eu}^{3+}-\text{Eu}^{2+}$ and $\text{Ce}^{4+}-\text{Ce}^{3+}$ valence states of Ce and Eu are more likely to replace Ca^{2+} in apatite due to the higher magmatic oxygen fugacity, the higher apatite $\text{Eu}^{3+}-\text{Eu}^{2+}$ ratio, and the lower $\text{Ce}^{4+}-\text{Ce}^{3+}$ ratio [64,65]. Eu and Ce show opposite behaviors in response to the change of the oxidation state in apatite. Therefore, the combination of the two elements is more reliable than using Eu anomalies alone [10]. Apatite from granitic magma in Darongxi has high negative Eu anomalies with $\delta\text{Eu} = 0.06$ – 0.12 and an average

value of 0.09, as well as having low positive Ce anomalies with $\delta\text{Ce} = 1.09\sim 1.13$ and an average value of 1.12, thus suggesting that the magma of the Darongxi mining area has a low oxygen fugacity and is formed in a reduced environment. The calculation results of oxygen fugacity from magmatic apatite are consistent with those of magmatic zircon, as well as with the evidence of reduced minerals in the granite, such as magmatic ilmenite (Figure 5j).

Halogens in apatite diffuse very slowly in magmatic systems, so the subsolid line halogen exchange does not affect its distribution behavior in apatite [66]. Strong enrichment or the loss of F and Cl in granite melts are not affected by apatite crystallization [67]. The concentration of F and Cl in magma can be evaluated using the concentration of F and Cl in apatite, which in turn provide information regarding the source of magma [68]. The magmatic apatite in Darongxi have high F concentrations (between 2.4 and 3.3 wt%, with an average of 2.7 wt%) and low Cl concentrations (between 0.002 and 0.050 wt%, with an average of 0.014 wt%), which reflect the characteristics of high F and low Cl in the magma (Figure 12). The granitic magma formed via the partial melting of the crust is generally low in Cl concentration, due to the sediment commonly losing more Cl than F during weathering [69]. The arc magma with metasomatic mantle wedge melting generally has a high concentration of F and Cl, due to plate dehydration releasing Cl-rich fluid into the arc magma. The low Cl concentration of the magma in the Darongxi mining area indicates that the magma source area may have derived from the partial melting of crust.

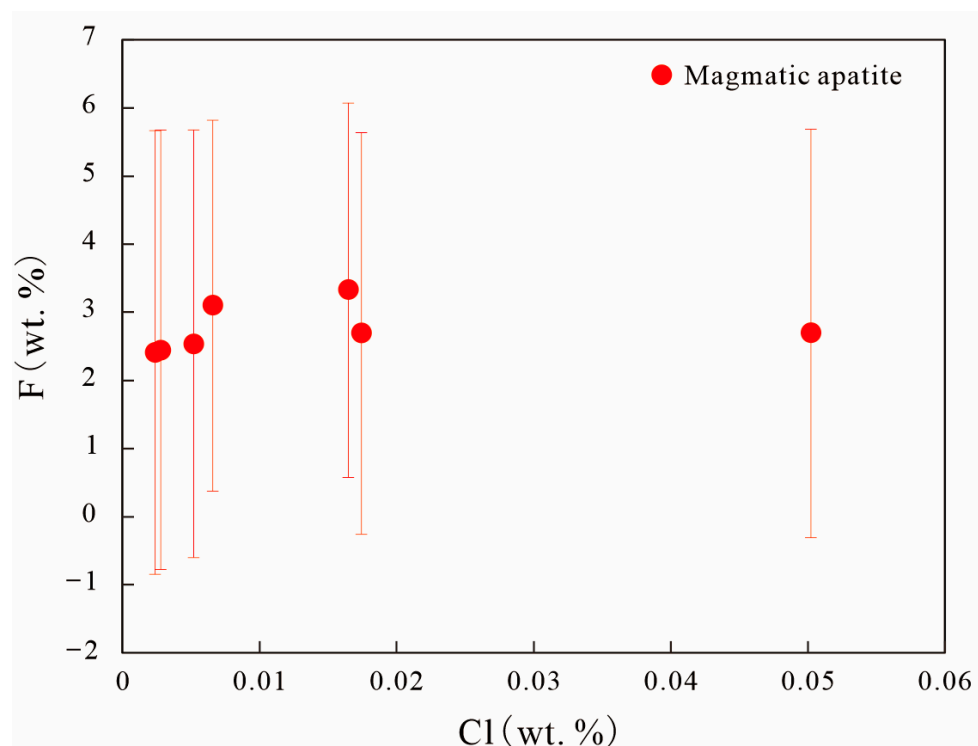


Figure 12. Magmatic apatite F-Cl diagram.

5.3. Coupling Relationship between Magma and Mineralization

The formation of W deposits related to magmatic rocks is controlled by many factors, such as the magmatic redox state, the magma source, and the concentration of halogen [70–72]. For example, skarn W-F-Sn deposits are often formed in reduced fluid environments, while skarn W-Cu-Mo deposits are often formed in oxidized fluid environments [73]. The garnets from the Darongxi deposit are rich in almandine-spessartine and poor in grossular, and the Mo concentration in scheelite is very low (0.02%), indicating that the Darongxi deposit was formed in a reduced environment [21]. The ore-bearing magma in Darongxi was also reduced, making this favorable for the formation of the

Darongxi W deposit. In addition, in felsic magma, W is mainly dissolved in W^{6+} when the oxygen fugacity is higher than IW (Iron-Wustite buffer), and W^{4+} exists only under extreme reduced conditions [74–76]. The overall oxygen fugacity of the magma in Darongxi is lower than that of the FMQ buffer, indicating that W is more likely to be in the +6 valence state, which is necessary for the formation of W in the later fluid exsolution.

As discussed above, the Hf isotopic composition of magmatic rocks and the characteristics of magmatic halogen show that the magmas in Darongxi are mainly derived from the partial melting of the Mesoproterozoic crust. The high concentration of W in the Dashenshan granite (595 ppm~849 ppm [35]) may indicate that the source of the magma is rich in W, which further supports the idea that the ore-forming materials of the Darongxi deposit may come from the W-enriched Mesoproterozoic crust.

The magmatic evolution of granite is very important for W mineralization, due to W being a highly incompatible lithophilic element [70,72]. Studies suggest that the F-rich melt has a low solid-phase line temperature, low viscosity, and a high diffusion coefficient, thereby having a positive effect on the mineral separation crystallization in the melt [77,78]. F-rich melts can also reduce the density of the melt and accelerate the process of gravitational differentiation between the crystal and the melt [71]. Therefore, the high F concentration of magma is an important factor in the promotion of magma evolution [79]. The high F concentration of the magma in Darongxi may prolong the magmatic evolution process, thus providing favorable conditions for W enrichment.

6. Conclusions

- (1) The Zircon U-Pb age of biotite monzonite granite, muscovite monzonite granite, and felsophyre in the Darongxi mining area ranged between 220.8 and 222.3 Ma, and $\epsilon_{\text{Hf}}(t)$ ranged from -2.2 to -8.1 , with the magma source mainly deriving from the Mesoproterozoic crust.
- (2) The ore-bearing magma in the Darongxi W deposit is reduced, as well as being rich in F and poor in Cl.
- (3) The reduced F-rich crust-source granitic rock and W-rich source provide favorable conditions for the mineralization of the Darongxi reduced skarn W deposit.

Supplementary Materials: The following supporting information can be downloaded at <https://www.mdpi.com/article/10.3390/min14030280/s1>: Table S1: Analysis conditions; Table S2: Zircon U-Pb age; Table S3: Zircon Lu-Hf isotope; Table S4: Zircon trace element; Table S5: Apatite major element; Table S6: Apatite trace element.

Author Contributions: Conceptualization and methodology, L.C., W.L. and G.X.; investigation, L.C., W.L. and G.X.; formal analysis, L.C. and F.Y.; writing—original draft preparation, L.C.; writing—review and editing, L.C., W.L. and G.X. All authors have read and agreed to the published version of the manuscript.

Funding: We acknowledge financial support from the National Science Foundation of China (grants 41925011, 42272073), and the Fundamental Research Funds for the Central Universities (2652021019).

Data Availability Statement: Data are contained within the article and Supplementary Materials.

Acknowledgments: We express our thanks to anonymous reviewers for their constructive comments, which significantly improved the manuscript. We are grateful to Hunan Chenzhou Mining Co., Ltd. for assistance during the investigation and the help of relevant experimental testing institutions and companies.

Conflicts of Interest: The authors declare no conflicts of interest.

References

1. Zhao, Y.M. Some New Important Advances in Study of Skarn Deposits. *Miner. Depos.* **2002**, *21*, 113–120. (In Chinese)
2. Newberry, R.J.; Swanson, S.E. Scheelite skarn granitoids: An evaluation of the roles of magmatic source and process. *Ore Geol. Rev.* **1986**, *1*, 57–81. [[CrossRef](#)]

3. Förster, H.J.; Tischendorf, G.; Trumbull, R.B.; Gottesmann, B. Late-collisional granites in the Variscan Erzgebirge, Germany. *J. Petrol.* **1999**, *40*, 1613–1645. [[CrossRef](#)]
4. Mao, J.W.; Cheng, Y.B.; Chen, G.H.; Franco, P. Major types and time–space distribution of Mesozoic ore deposits in South China and their geodynamic settings. *Miner. Depos.* **2013**, *48*, 267–294. [[CrossRef](#)]
5. Song, S.W.; Mao, J.W.; Xie, G.Q.; Song, H.; Chen, G.H.; Rao, J.F.; Ouyang, Y.P. Identification of ore-related granitic intrusions in W skarn deposits: A case study of giant Zhuxi W skarn deposit. *Miner. Depos.* **2018**, *37*, 940–960. (In Chinese)
6. Su, Q.W.; Mao, J.W.; Wu, S.H.; Zhang, Z.C.; Xu, S.F. Geochronology and geochemistry of the granitoids and ore-forming age in the Xiaoyao tungsten polymetallic skarn deposit in the Jiangnan Massif tungsten belt, China: Implications for their petrogenesis, geodynamic setting, and mineralization. *Lithos* **2018**, *296*, 365–381. [[CrossRef](#)]
7. Li, G.M.; Cao, M.J.; Qin, K.Z.; Evans, N.J.; Hollings, P.; Seitmuratova, E.Y. Geochronology, petrogenesis and tectonic settings of pre-and syn-ore granites from the W-Mo deposits (East Kounrad, Zhanet and Akshatau), Central Kazakhstan. *Lithos* **2016**, *252*, 16–31. [[CrossRef](#)]
8. Kong, Z.G.; Liang, T.; Mao, J.W.; Xu, S.F.; Xu, H.B.; Yan, P.P.; Jin, X.Y. Study on perogenesis of granodiorite, metallogenic epoch and petrogenetic-metallogenetic setting in the Zhuxiling tungsten polymetallic deposit, southern Anhui Province, China. *Acta Petrol. Sin.* **2018**, *34*, 2632–2656. (In Chinese)
9. Poitrenaud, T.; Poujol, M.; Augier, R.; Marcoux, E. The polyphase evolution of a late Variscan W/Au deposit (Salau, French Pyrenees): Insights from REE and U/Pb LA-ICP-MS analyses. *Miner. Depos.* **2020**, *55*, 1127–1147. [[CrossRef](#)]
10. Sun, S.J.; Yang, X.Y.; Wang, G.J.; Sun, W.D.; Zhang, H.; Li, C.Y.; Ding, X. In situ elemental and Sr-O isotopic studies on apatite from the Xu-Huai intrusion at the southern margin of the North China Craton: Implications for petrogenesis and metallogeny. *Chem. Geol.* **2019**, *510*, 200–214. [[CrossRef](#)]
11. Wang, L.X.; Ma, C.Q.; Zhang, C.; Zhu, Y.X.; Marks, M.A. Halogen geochemistry of I- and A-type granites from Jiuhuashan region (South China): Insights into the elevated fluorine in A-type granite. *Chem. Geol.* **2018**, *478*, 164–182. [[CrossRef](#)]
12. Harlov, D.E. Apatite: A fingerprint for metasomatic processes. *Elements* **2015**, *11*, 171–176. [[CrossRef](#)]
13. Li, W.; Xie, G.Q.; Mao, J.W.; Cook, N.J.; Wei, H.T.; Ji, Y.H.; Fu, B. Precise age constraints for the Woxi Au-Sb-W deposit, south China. *Econ. Geol.* **2023**, *118*, 509–518. [[CrossRef](#)]
14. Hu, A.X.; Peng, J.T. Fluid inclusions and ore precipitation mechanism in the giant Xikuangshan mesothermal antimony deposit, South China: Conventional and infrared microthermometric constraints. *Ore Geol. Rev.* **2018**, *95*, 49–64. [[CrossRef](#)]
15. Wang, C.; Peng, J.T.; Xu, J.B.; Yang, J.H.; Hu, A.X.; Chen, X.J. Petrogenesis and metallogenic effect of the Baimashan granitic complex in central Hunan, South China. *Acta Petrol. Sin.* **2021**, *37*, 805–829. (In Chinese) [[CrossRef](#)]
16. Lu, Y.L.; Peng, J.T.; Yang, J.H.; Hu, A.X.; Li, Y.K.; Tan, H.Y.; Xiao, Q.Y. Petrogenesis of the Ziyunshan pluton in central Hunan, South China: Constraints from zircon U-Pb dating, element geochemistry and Hf-O isotopes. *Acta Petrol. Sin.* **2017**, *33*, 1705–1728. (In Chinese)
17. Fu, S.L.; Hu, R.Z.; Bi, X.W.; Chen, Y.W.; Yang, J.H.; Huang, Y. Origin of Triassic granites in central Hunan Province, South China: Constraints from zircon U–Pb ages and Hf and O isotopes. *Int. Geol. Rev.* **2015**, *57*, 97–111. [[CrossRef](#)]
18. Loucks, R.R.; Fiorentini, M.L.; Henríquez, G.J. New magmatic oxybarometer using trace elements in zircon. *J. Petrol.* **2020**, *61*, ega034. [[CrossRef](#)]
19. Ferry, J.M.; Watson, E.B. New thermodynamic models and revised calibrations for the Ti-in-zircon and Zr-in-rutile thermometers. *Contrib. Mineral. Petrol.* **2007**, *154*, 429–437. [[CrossRef](#)]
20. Ballard, J.R.; Palin, M.J.; Campbell, I.H. Relative oxidation states of magmas inferred from Ce (IV)/Ce (III) in zircon: Application to porphyry copper deposits of northern Chile. *Contrib. Mineral. Petrol.* **2002**, *144*, 347–364. [[CrossRef](#)]
21. Zhang, L.S.; Peng, J.T.; Lin, F.M. Mineralogical, geochemical characteristics and formation mechanism of skarn minerals in the Darongxi tungsten deposit, western Hunan. *Geol. Rev.* **2020**, *66*, 113–139. (In Chinese)
22. Xue, H.M. Geochronology, geochemistry and stratospheric interactions of Late Mesozoic granitoids near the boundary between Anhui and Zhejiang provinces in the eastern segment of the Jiangnan orogenic belt. *Acta Petrol. Sin.* **2021**, *37*, 433–461. (In Chinese) [[CrossRef](#)]
23. Dong, G.J.; Xu, D.R.; Wang, L.; Chen, G.H.; He, Z.L.; Fu, G.G.; Wu, J.; Wang, Z.L. Determination of mineralizing ages on gold ore deposits in the eastern Hunan province, south China and Isotopic tracking on ore-forming fluids—re-discussing gold ore deposit. *Geotecton. Metallog.* **2008**, *32*, 482–491.
24. Li, X.Y.; Lu, J.J.; Zhang, R.Q.; Gao, J.F.; Wu, J.W. Magma evolution leading to veinlet-disseminated tungsten mineralization at the Muguayuan deposit: In-situ analysis of igneous minerals. *Ore Geol. Rev.* **2021**, *138*, 104406. [[CrossRef](#)]
25. Zhang, S.T.; Zhang, R.Q.; Lu, J.J.; Ma, D.S.; Ding, T.; Gao, S.Y.; Zhang, Q. Neoproterozoic tin mineralization in South China: Geology and cassiterite U–Pb age of the Baotan tin deposit in northern Guangxi. *Miner. Depos.* **2019**, *54*, 1125–1142. [[CrossRef](#)]
26. Song, S.W.; Mao, J.W.; Xie, G.Q.; Lehmann, B.; Jian, W.; Wang, X.G. The world-class mid-Mesozoic Jiangnan tungsten belt, South China: Coeval large reduced and small oxidized tungsten systems controlled by different magmatic petrogeneses. *Ore Geol. Rev.* **2021**, *139*, 104543. [[CrossRef](#)]
27. Li, W.; Cook, N.J.; Xie, G.Q.; Mao, J.W.; Ciobanu, C.L.; Li, J.W.; Zhang, Z.Y. Textures and trace element signatures of pyrite and arsenopyrite from the Gutaishan Au–Sb deposit, South China. *Miner. Depos.* **2019**, *54*, 591–610. [[CrossRef](#)]

28. Li, J.K.; Liu, Y.C.; Zhao, Z.; Chou, I.M. Roles of carbonate/CO₂ in the formation of quartz-vein wolframite deposits: Insight from the crystallization experiments of huebnerite in alkali-carbonate aqueous solutions in a hydrothermal diamond-anvil cell. *Ore Geol. Rev.* **2018**, *95*, 40–48. [[CrossRef](#)]
29. Hu, R.Z.; Fu, S.L.; Huang, Y.; Zhou, M.F.; Fu, S.H.; Zhao, C.H.; Wang, Y.J.; Bi, X.W.; Xiao, J.F. The giant South China Mesozoic low-temperature metallogenic domain: Reviews and a new geodynamic model. *J. Asian Earth Sci.* **2017**, *137*, 9–34. [[CrossRef](#)]
30. Xie, G.Q.; Mao, J.W.; Bagas, L.; Fu, B.; Zhang, Z.Y. Mineralogy and titanite geochronology of the Caojiaba W deposit, Xiangzhong metallogenic province, southern China: Implications for a distal reduced skarn W formation. *Miner. Depos.* **2019**, *54*, 459–472. [[CrossRef](#)]
31. Su, K.M.; Lu, S.J.; Kong, L.B.; Yang, F.Q.; Xiang, J.F. Geological characteristics, metallogenic regularity and model of quartz vein type tungsten deposits in Chongyangping, Hunan Province. *Miner. Depos.* **2016**, *35*, 902–912. (In Chinese)
32. Li, W.; Xie, G.Q.; Mao, J.W.; Zhang, H.C. Mineralogy, fluid inclusion and isotope signatures: Implications for the genesis of the Early Paleozoic Yangjiashan scheelite-quartz vein deposit, South China. *Ore Geol. Rev.* **2021**, *134*, 104136. [[CrossRef](#)]
33. Xie, G.Q.; Mao, J.W.; Li, W.; Fu, B.; Zhang, Z.Y. Granite-related Yangjiashan tungsten deposit, southern China. *Miner. Depos.* **2019**, *54*, 67–80. [[CrossRef](#)]
34. Zhang, L.S.; Peng, J.T.; Hu, A.X.; Lin, F.M.; Zhang, T. Re-Os dating of molybdenite from Darongxi tungsten deposit in Western Hunan and its geological implications. *Miner. Depos.* **2014**, *33*, 181–189. (In Chinese)
35. Xu, H.J.; Ma, C.Q.; Zhao, J.H.; Zhang, J.F. Petrogenesis of Dashenshan I-type granodiorite: Implications for Triassic crust–mantle interaction, South China. *Int. Geol. Rev.* **2014**, *56*, 332–350. [[CrossRef](#)]
36. Zhang, L.S.; Peng, J.T.; Zhang, D.L.; Hu, A.X.; Yang, J.H. Geochemistry and Petrogenesis of the Indosinian Dashenshan Granite, Western Hunan, South China. *Geotecton. Metallog.* **2012**, *36*, 137–148. (In Chinese)
37. Shan, L.; Pang, Y.C.; Ke, X.Z.; Liu, J.J.; Chen, W.H.; Niu, Z.J.; Xu, D.M.; Long, W.G.; Wang, B.Q. Diagenetic and Metallogenic Age of the Muguayuan Tungsten Polymetallic Deposit and Its Effect on Regional Mineralization, Taojiang County, Northeastern Hunan Province, China. *Geol. Sci. Technol. Inf.* **2019**, *38*, 100–112. (In Chinese)
38. Xu, H.J.; Ma, C.Q.; Zhao, J.H.; Zhang, J.F. Magma mixing generated Triassic I-type granites in South China. *J. Geol.* **2014**, *122*, 329–351. [[CrossRef](#)]
39. Lv, Y.J.; Peng, J.; Cai, Y.F. Geochemical characteristics, U-Pb dating of hydrothermal titanite from the Xingfengshan tungsten deposit in Hunan Province and their geological significance. *Acta Petrol. Sin.* **2021**, *37*, 830–846. (In Chinese) [[CrossRef](#)]
40. Peng, J.T.; Wang, C.; Li, Y.K.; Hu, A.X.; Lu, Y.L.; Chen, X.J. Geochemical characteristics and Sm-Nd geochronology of scheelite in the Baojinshan ore district, central Hunan. *Acta Petrol. Sin.* **2021**, *37*, 665–682. (In Chinese) [[CrossRef](#)]
41. Zhang, Z.Y.; Xie, G.Q.; Thompson, J. Skarn mineralogy and in-situ LA-ICP-MS U-Pb geochronology of wolframite for the Caojiaba tungsten deposit, southern China: Implications for a reduced tungsten skarn deposit. *Ore Geol. Rev.* **2022**, *147*, 104981. [[CrossRef](#)]
42. Wang, Y.L.; Chen, Y.C.; Wang, D.H.; Xu, J.; Chen, Z.H. Scheelite Sm-Nd dating of the Zhazixi W-Sb deposit in Hunan and its geological significance. *Geol. China* **2012**, *39*, 1339–1344. (In Chinese)
43. Bai, D.Y.; Wu, N.J.; Zhong, X.; Jia, P.Y.; Xiong, X.; Huang, W.Y. Geochronology, Petrogenesis and Tectonic Setting of Indosinian Wawutang Granites, Southwestern Hunan Province. *Geotecton. Metallog.* **2016**, *40*, 1075–1091. (In Chinese)
44. Wang, K.X.; Chen, W.F.; Chen, P.R.; Ling, H.F.; Huang, H. Petrogenesis and geodynamic implications of the Xiema and Ziyunshan plutons in Hunan Province, South China. *J. Asian Earth Sci.* **2015**, *111*, 919–935. [[CrossRef](#)]
45. Wiedenbeck, M.; Alle, P.; Corfu, F.Y.; Griffin, W.L.; Meier, M.; Oberli, F.V.; Quadt, A.V.; Roddick, J.C.; Spiegel, W. Three natural zircon standards for U-Th-Pb, Lu-Hf, trace element and REE analyses. *Geostand. Newsl.* **1995**, *19*, 1–23. [[CrossRef](#)]
46. Sláma, J.; Košler, J.; Condon, D.J.; Crowley, J.L.; Gerdes, A.; Hanchar, J.M.; Horstwood, M.S.A.; Morris, G.A.; Nasdala, L.; Norberg, N.; et al. Plešovice zircon—A new natural reference material for U–Pb and Hf isotopic microanalysis. *Chem. Geol.* **2008**, *249*, 1–35. [[CrossRef](#)]
47. Ludwig, K.R. ISOPLOT 3.0: A Geochronological Toolkit for Microsoft Excel. Berkeley Geochronol. Cent. Spec. Publ. **2003**, *4*, 70.
48. Hu, Z.C.; Li, X.H.; Luo, T.; Zhang, W.; Crowley, J.; Li, Q.L.; Ling, X.X.; Yang, C.; Li, Y.; Feng, L.P.; et al. Tanz zircon megacrysts: A new zircon reference material for the microbeam determination of U–Pb ages and Zr–O isotopes. *J. Anal. At. Spectrom.* **2021**, *36*, 2715–2734. [[CrossRef](#)]
49. Chu, N.C.; Taylor, R.N.; Chavagnac, V.; Nesbitt, R.W.; Boella, R.M.; Milton, J.A.; German, C.R.; Bayon, G.; Burton, K. Hf isotope ratio analysis using multi-collector inductively coupled plasma mass spectrometry: An evaluation of isobaric interference corrections. *J. Anal. At. Spectrom.* **2002**, *17*, 1567–1574. [[CrossRef](#)]
50. Hou, K.J.; Li, Y.H.; Zou, T.R.; Qu, X.M.; Shi, Y.R.; Xie, G.Q. Laser ablation-MC-ICP-MS technique for Hf isotope microanalysis of zircon and its geological applications. *Acta Petrol. Sin.* **2007**, *23*, 2595–2604. (In Chinese)
51. Wu, F.Y.; Yang, Y.H.; Xie, L.W.; Yang, J.H.; Xu, P. Hf isotopic compositions of the standard zircons and baddeleyites used in U-Pb geochronology. *Chem. Geol.* **2006**, *234*, 105–126. [[CrossRef](#)]
52. Morel, M.L.A.; Nebel, O.; Nebel-Jacobsen, Y.J.; Miller, J.S.; Vroon, P.Z. Hafnium isotope characterization of the GJ-1 zircon reference material by solution and laser-ablation MC-ICPMS. *Chem. Geol.* **2008**, *255*, 231–235. [[CrossRef](#)]
53. Hu, Z.C.; Zhang, W.; Liu, Y.S.; Gao, S.; Li, M.; Zong, K.Q.; Chen, H.H.; Hu, S.H. “Wave” Signal-Smoothing and Mercury-Removing Device for Laser Ablation Quadrupole and Multiple Collector ICPMS Analysis: Application to Lead Isotope Analysis. *Anal. Chem.* **2015**, *87*, 1152–1157. [[CrossRef](#)] [[PubMed](#)]

54. Liu, Y.S.; Hu, Z.C.; Gao, S.; Günther, D.; Xu, J.; Gao, C.G.; Chen, H.H. In situ analysis of major and trace elements of anhydrous minerals by LA-ICP-MS without applying an internal standard. *Chem. Geol.* **2008**, *257*, 34–43. [[CrossRef](#)]
55. Sun, S.S.; McDonough, W.F. Chemical and isotopic systematics of oceanic basalts: Implications for mantle composition and processes. *Geol. Soc. Lond. Spec. Publ.* **1989**, *42*, 313–345. [[CrossRef](#)]
56. Wang, K.X.; Chen, P.R.; Chen, W.F.; Ling, H.F.; Zhao, K.D.; Yu, Z.Q. Magma mingling and chemical diffusion in the Taojiang granitoids in the Hunan Province, China: Evidences from petrography, geochronology and geochemistry. *Mineral. Petrol.* **2012**, *106*, 243–264. [[CrossRef](#)]
57. Lu, Y.L.; Peng, J.T.; Yang, J.H.; Li, Y.K.; Chen, X.J.; Zhou, X.; Li, G.L. Zircon U-Pb ages and Hf-O isotopes of granodiorite -porphyry in Baojinshan mining area and their geological significance. *Chin. J. Nonferrous Met.* **2017**, *27*, 1441–1454. (In Chinese)
58. Watson, E.B.; Wark, D.A.; Thomas, J.B. Crystallization thermometers for zircon and rutile. *Contrib. Mineral. Petrol.* **2006**, *151*, 413–433. [[CrossRef](#)]
59. Zhang, L.P.; Zhang, R.Q.; Wu, K.; Chen, Y.X.; Li, C.Y.; Hu, Y.B.; He, J.J.; Liang, J.L.; Sun, W.D. Late Cretaceous granitic magmatism and mineralization in the Yingwuling W-Sn deposit, South China: Constraints from zircon and cassiterite U-Pb geochronology and whole-rock geochemistry. *Ore Geol. Rev.* **2018**, *96*, 115–129. [[CrossRef](#)]
60. Lu, Y.J.; Loucks, R.R.; Fiorentini, M.; McCuaig, T.C.; Evans, N.J.; Yang, Z.M.; Hou, Z.Q.; Kirkland, C.L.; Parra-Avila, L.A.; Kobussen, A. *Zircon Compositions as a Pathfinder for Porphyry Cu±Mo±Au Deposits*; Society of Economic Geologists, Special Publication: Littleton, CO, USA, 2016; pp. 329–347.
61. Zou, X.Y.; Jiang, J.L.; Qin, K.Z.; Zhang, Y.G.; Yang, W.; Li, X.H. Progress in the principle and application of zircon trace element. *Acta Petrol. Sin.* **2021**, *37*, 985–999. (In Chinese) [[CrossRef](#)]
62. Trail, D.; Watson, E.B.; Tailby, N.D. Ce and Eu anomalies in zircon as proxies for the oxidation state of magmas. *Geochim. Cosmochim. Acta* **2012**, *97*, 70–87. [[CrossRef](#)]
63. Trail, D.; Watson, E.B.; Tailby, N.D. The oxidation state of Hadean magmas and implications for early Earth's atmosphere. *Nature* **2011**, *480*, 79–82. [[CrossRef](#)] [[PubMed](#)]
64. Pan, Y.M.; Fleet, M.E. Compositions of the apatite-group minerals: Substitution mechanisms and controlling factors. *Rev. Mineral. Geochem.* **2002**, *48*, 13–49. [[CrossRef](#)]
65. Sha, L.K.; Chappell, B.W. Apatite chemical composition, determined by electron microprobe and laser-ablation inductively coupled plasma mass spectrometry, as a probe into granite petrogenesis. *Geochim. Cosmochim. Acta* **1999**, *63*, 3861–3881. [[CrossRef](#)]
66. Piccoli, P.; Candela, P. Apatite in felsic rocks; a model for the estimation of initial halogen concentrations in the Bishop Tuff (Long Valley) and Tuolumne Intrusive Suite (Sierra Nevada Batholith) magmas. *Am. J. Sci.* **1994**, *294*, 92–135. [[CrossRef](#)]
67. Zhang, C.; Holtz, F.; Ma, C.Q.; Wolff, P.E.; Li, X.Y. Tracing the evolution and distribution of F and Cl in plutonic systems from volatile-bearing minerals: A case study from the Liujiawa pluton (Dabie orogen, China). *Contrib. Mineral. Petrol.* **2012**, *164*, 859–879. [[CrossRef](#)]
68. Doherty, A.L.; Webster, J.D.; Goldoff, B.A.; Piccoli, P.M. Partitioning behavior of chlorine and fluorine in felsic melt–fluid(s)–apatite systems at 50MPa and 850–950 °C. *Chem. Geol.* **2014**, *384*, 94–111. [[CrossRef](#)]
69. Blevin, P.L.; Chappell, B.W. Chemistry, origin, and evolution of mineralized granites in the Lachlan fold belt, Australia; the metallogeny of I- and S-type granites. *Econ. Geol.* **1995**, *90*, 1604–1619. [[CrossRef](#)]
70. Huang, L.C.; Jiang, S.Y. Highly fractionated S-type granites from the giant Dahutang tungsten deposit in Jiangnan Orogen, Southeast China: Geochronology, petrogenesis and their relationship with W-mineralization. *Lithos* **2014**, *202–203*, 207–226. [[CrossRef](#)]
71. Dingwell, D.B.; Knoche, R.; Webb, S.L. The effect of F on the density of haplogranite melt. *Am. Miner.* **1993**, *78*, 325–330.
72. Groves, D.I.; McCarthy, T.S. Fractional crystallization and the origin of tin deposits in granitoids. *Miner. Depos.* **1978**, *13*, 11–26. [[CrossRef](#)]
73. Newberry, R. Tectonic and geochemical setting of tungsten skarn mineralization in the Cordillera. *Ariz. Geol. Soc. Digest.* **1981**, *14*, 99–111.
74. Che, X.D.; Linnen, R.L.; Wang, R.C.; Groat, L.A.; Brand, A.A. Distribution of trace and rare earth elements in titanite from tungsten and molybdenum deposits in Yukon and British Columbia, Canada. *Can. Miner.* **2013**, *51*, 415–438. [[CrossRef](#)]
75. Wade, J.; Wood, B.J.; Norris, C.A. The oxidation state of tungsten in silicate melt at high pressures and temperatures. *Chem. Geol.* **2013**, *335*, 189–193. [[CrossRef](#)]
76. O'Neill, H.S.C.; Berry, A.J.; Eggins, S.M. The solubility and oxidation state of tungsten in silicate melts: Implications for the comparative chemistry of W and Mo in planetary differentiation processes. *Chem. Geol.* **2008**, *255*, 346–359. [[CrossRef](#)]
77. Dingwell, D.B.; Webb, S.L. The fluxing effect of fluorine at magmatic temperatures (600–800 °C): A scanning calorimetric study. *Am. Miner.* **1992**, *77*, 30–33.
78. Dingwell, D.B.; Scarfe, C.M.; Cronin, D.J. The effect of fluorine on viscosities in the system Na₂O–Al₂O₃–SiO₂: Implications for phonolites, trachytes and rhyolites. *Am. Miner.* **1985**, *70*, 80–87.
79. Zhu, H.L.; Zhang, L.P.; Du, L.; Sui, Q.L. The geochemical behavior of tungsten and the genesis of tungsten deposits in South China. *Acta Petrol. Sin.* **2020**, *36*, 13–22. (In Chinese) [[CrossRef](#)]

Disclaimer/Publisher's Note: The statements, opinions and data contained in all publications are solely those of the individual author(s) and contributor(s) and not of MDPI and/or the editor(s). MDPI and/or the editor(s) disclaim responsibility for any injury to people or property resulting from any ideas, methods, instructions or products referred to in the content.